A&A 594, A78 (2016)
DOI: 10.1051/0004-6361/201628609

Astronomy & Astrophysics

Suzaku and *XMM-Newton* observations of the North Polar Spur: Charge exchange or ISM absorption?

Liyi Gu[1], Junjie Mao[1], Elisa Costantini[1], and Jelle Kaastra[1,2]

[1] SRON Netherlands Institute for Space Research, Sorbonnelaan 2, 3584 CA Utrecht, The Netherlands
e-mail: L.Gu@sron.nl
[2] Leiden Observatory, Leiden University, PO Box 9513, 2300 RA Leiden, The Netherlands

Received 30 March 2016 / Accepted 27 July 2016

ABSTRACT

By revisiting the *Suzaku* and *XMM-Newton* data of the North Polar Spur, we discovered that the spectra are inconsistent with the traditional model consisting of pure thermal emission and neutral absorption. The most prominent discrepancies are the enhanced O VII and Ne IX forbidden-to-resonance ratios, and a high O VIII Lyβ line relative to other Lyman series. A collisionally ionized absorption model can naturally explain both features, while a charge exchange component can only account for the former. By including the additional ionized absorption, the plasma in the North Polar Spur can be described by a single-phase collisional ionization equilibrium (CIE) component with a temperature of 0.25 keV, and nitrogen, oxygen, neon, magnesium, and iron abundances of 0.4−0.8 solar. The abundance pattern of the North Polar Spur is well in line with those of the Galactic halo stars. The high nitrogen-to-oxygen ratio reported in previous studies can be migrated to the large transmission of the O VIII Lyα line. The ionized absorber is characterized by a balance temperature of 0.17−0.20 keV and a column density of $3-5 \times 10^{19}$ cm^{-2}. Based on the derived abundances and absorption, we speculate that the North Polar Spur is a structure in the Galactic halo, so that the emission is mostly absorbed by the Galactic interstellar medium in the line of sight.

Key words. ISM: structure – ISM: individual objects: North Polar Spur – ISM: abundances – X-rays: ISM

1. Introduction

The North Polar Spur (NPS) is a prominent structure emitting both in the soft X-ray and radio bands, with a projected distribution from the Galactic plane at $l \sim 20°$ toward the north Galactic pole. Despite its vicinity, the origin of the NPS remains largely unclear. Early research suggested that the NPS is an old supernova remnant, or a front created by stellar wind from the Scorpio-Centaurus OB association, at a distance of several hundred pc from the Sun (Berkhuijsen et al. 1971; Egger & Aschenbach 1995). Alternatively, the NPS can be explained as a shock front produced by an energetic event, such as starburst, in the Galactic center ∼15 Myr ago (Sofue et al. 1977; Bland-Hawthorn & Cohen 2003). Recent morphological studies further indicated a possible relation between the NPS and the *Fermi* γ-ray bubbles (e.g., Kataoka et al. 2013). In the Galactic center origin scenario, the distance to the NPS is expected to be several kpc.

X-ray studies of the NPS hot plasma provide important information, including the plasma temperature, density, and metal abundances, which are essential to understand its origin. Using *XMM-Newton* observations of three regions in the NPS, Willingale et al. (2003, hereafter W03) identified a thermal component, with a temperature of ≈0.26 keV and metal abundances of ∼0.5 $Z_\odot$, associated with the enhanced NPS emission. They further deduced that the thermal energy contained in the NPS is consistent with the energy released by one or more supernovae events. Based on a *Suzaku* observation, Miller et al. (2008, hereafter M08) measured a slightly higher thermal temperature of ∼0.30 keV and a quite enhanced nitrogen abundance, with a nitrogen-to-oxygen abundance ratio ≈4.0 times of the solar value. They proposed that additional enrichment from stellar evolution in the NPS vicinity is required to explain the observed abundance pattern.

The above two X-ray studies are both based on an assumption that the NPS emission purely stems from thermal plasma in collisional ionization equilibrium (CIE), affected by only neutral absorption in the line of sight. Recent research shows that some diffuse objects also emit non-thermal X-rays, such as charge exchange emission produced at the interface between hot and cold materials (e.g., Lisse et al. 1996; Katsuda et al. 2011; Gu et al. 2015). There are also cases in which a portion of the foreground absorber appears to be highly ionized, as reported in Yao & Wang (2005) and Hagihara et al. (2010, 2011), for example. Both the charge exchange component and ionized absorption can strongly affect the line emission, and hence deviate from the resulting physical model. The NPS is a potential target for charge exchange because it might be surrounded by a shell of neutral gas (e.g., Heiles et al. 1980), providing substantial environment for ion-neutral charge exchange. Meanwhile, the NPS might be subject to ionized absorption, since it is expected in the Galactic center origin scenario to be located behind a layer of hot interstellar medium (ISM) of the Galactic halo or bulge. The spectra presented in W03 and M08 have shown a hint for such additional components: the central line energies of unresolved O VII and Ne IX triplets are shifted by a few 10 eV to longer wavelengths, relative to the energies of O VIII and Ne X (Lallement 2009). This might indicate either charge-exchange enhancement of the forbidden lines, or possible absorption in the resonance ones.

In this paper, we present a detailed spectral analysis by revisiting the high-quality X-ray data of the NPS. The latest SPEX

version 3.01 is employed because it includes a new charge-exchange code (Gu et al. 2016) and a model for ionized absorption. Section 2 briefly describes the data reduction, and the data analysis and results are presented in Sect. 3. We discuss the physical implication of the results in Sect. 4 and summarize our work in Sect. 5. Throughout the paper, the errors are given at a 68% confidence level. We adopt the proto-solar abundance table of Lodders et al. (2009) and convert the previous abundance measurements to the new standard.

2. Observations and data reduction

2.1. Suzaku and XMM-Newton datasets

The NPS region was observed by *Suzaku*, pointing at Galactic coordinates $l = 26.83°$ and $b = 21.95°$, on 2005 October 3 for a total exposure of 46.1 ks. The same XIS dataset was already used in M08. The data were processed with the latest HEASoft 6.18 and CALDB 151005. Following Gu et al. (2012), we removed hot pixels and data obtained either near the South Atlantic Anomaly or at low elevation angles from the Earth rim. For each XIS detector, a 0.3−8.0 keV light curve was extracted from a source-free region and was screened to filter off anomalously high count bins with rates above the 2σ limit of the quiescent mean value. The XIS0 and XIS1 data are affected by high count rate periods over 3σ of the mean value, probably due to a temporary system anomaly and variation in the particle background. Some periods with high particle counts are also visible in the XIS2 and XIS3 light curves. The clean exposures are 37 ks, 38 ks, 40 ks, and 40 ks for the XIS0, XIS1, XIS2, and XIS3 data, respectively. Similar time filtering results were reported in M08. Contaminating point sources were masked out in the same way as in M08.

XMM-Newton was used to observe six fields of the NPS region; as reported in W03, only three datasets (fields IV, V, and VI) are suitable, providing a total exposure of 45.7 ks. The three pointings have Galactic coordinates $(l, b) = (25°, 20°)$, $(20°, 30°)$, and $(20°, 40°)$. The SAS v13.5 and the built-in extended source analysis software (ESAS) were used to process and calibrate the data obtained with the *XMM-Newton* European Photon Imaging Camera (EPIC). The MOS raw data were created by `emchain`, and the light curves were extracted and screened for time-variable background components by the `mos-filter` task, which uses filter of 2σ as a conservative cut. The final net clean exposures are 13 ks, 12 ks, and 13 ks for fields IV, V, and VI, respectively. The point sources were detected and removed by the task `cheese` with a flux threshold of 10^{-14} erg cm^{-2} s^{-1}; the field IV is also contaminated by a diffuse X-ray source and it was masked out manually. The spectra and response files were calculated by the `mos-spectra` mask. The pn data are not included in this work, since they suffered more from the time-variable particle background and have a lower spectral resolution than the MOS data in the soft X-ray band.

2.2. Background modeling

The background was estimated to be a combination of three components: non X-ray background (NXB), cosmic X-ray background (CXB), and Galactic emission. For the XIS and MOS datasets, the NXB spectra were created by the `xisnxbgen` and `mos-back` tasks, which are based on a darkEarth observation and exposures with a closed filter wheel, respectively. To determine the CXB and Galactic components, we analyzed an off-source XIS pointing in the direction of the intermediate polar 1RXS J180340.0+40121 at Galactic $l = 66.85°$ and $b = 25.78°$. This object is clearly outside the NPS structure and has a similar Galactic latitude as the NPS XIS pointing. It is therefore best suited for characterizing the background of the NPS structure. The data were screened in the same way as described in Sect. 2.1. After excluding the central 4′ region covering the intermediate polar and subtracting the NXB based on dark-Earth observation, we performed a model fitting of the remaining spectrum with the CXB and Galactic components. The CXB was approximated by a broken power-law with photon indices $\Gamma = 2.0$ and 1.4 at <0.7 keV and >0.7 keV bands, respectively, absorbed by the Galactic cold material with a column density of 3.54×10^{20} cm^2 (Willingale et al. 2013). The Galactic emission consists of two sub-components: the local hot bubble (LHB) and Galactic halo (GH) emissions. We included an unabsorbed, solar-abundance `CIE` component with a fixed temperature of 0.08 keV to account for the LHB emission, and another absorbed brighter `CIE` component with a temperature of 0.2 keV and solar abundance for the GH. The off-source XIS spectra can be well fit by the model, with C-statistics of 215 for 182 degrees of freedom. The best-fit CXB flux is 7.2×10^{-8} erg cm^{-2} s^{-1} sr^{-1} in 2−10 keV, which agrees well with previous reports (e.g., Gu et al. 2012). The best-fit CXB and Galactic backgrounds were then used in the subsequent NPS analysis.

Errors quoted in our spectral analysis were estimated by accounting for statistical and systematic uncertainties. The former were calculated by the `SPEX` command `error`, as the fitting was repeated for several iterations to ensure that we found the lowest C-statistics is found. For the latter, the NXB, CXB, LHB, and GH components were renormalized by 10% to assess the typical background error.

3. Analysis and results

3.1. `CIE` and `CX` with neutral absorption

After subtracting the point sources and background, we first fit the full-field XIS and MOS spectra by a single-phase `CIE` component, absorbed by only neutral material. For each field, the absorbing column density was allowed to vary up to the Galactic value given in Willingale et al. (2013). The plasma emission measure, temperature, and N, O, Ne, Mg, and Fe abundances were also left free. The fitting was performed over the 0.4−3.0 keV for both XIS and MOS data. The best-fit models are plotted in Fig. 1. As was noted in M08, the XIS spectra in the 0.5−1.0 keV are poorly fit with this simple model (C-statistics = 1152.9 for a degree of freedom of 717). Apparent residuals are visible in the O VII Heα (0.56−0.57 keV), Ne IX Heα (0.90−0.92 keV) and O VIII Lyβ (0.77 keV) bands. At the first two energies, the emission from the unresolved He-like triplets appears to be systematically shifted, by 10−20 eV, to the forbidden line side, while the H-like Lyα counterparts are nicely fit by the thermal model. For the O VIII Lyβ line, the `CIE` model underestimates the line intensity by ∼20%, which indicates an anomalously high Lyβ/Lyα ratio. Adding another `CIE` component does not improve the fitting. The poor fit cannnot be caused by possible defects in the *Suzaku* calibration or atomic model (Appendix A). As shown in Table 1, the best-fit temperature is 0.27 ± 0.01 keV, the N and O abundances are $0.71 \pm 0.17\ Z_\odot$ and $0.25 \pm 0.03\ Z_\odot$, respectively, and the Ne, Mg, and Fe abundances are about $0.3-0.6\ Z_\odot$. These results agree well with those reported in M08.

As plotted in Figs. 1b−d, the MOS spectra are fit with the CIE model with a neutral absorber, and the obtained C-statistics

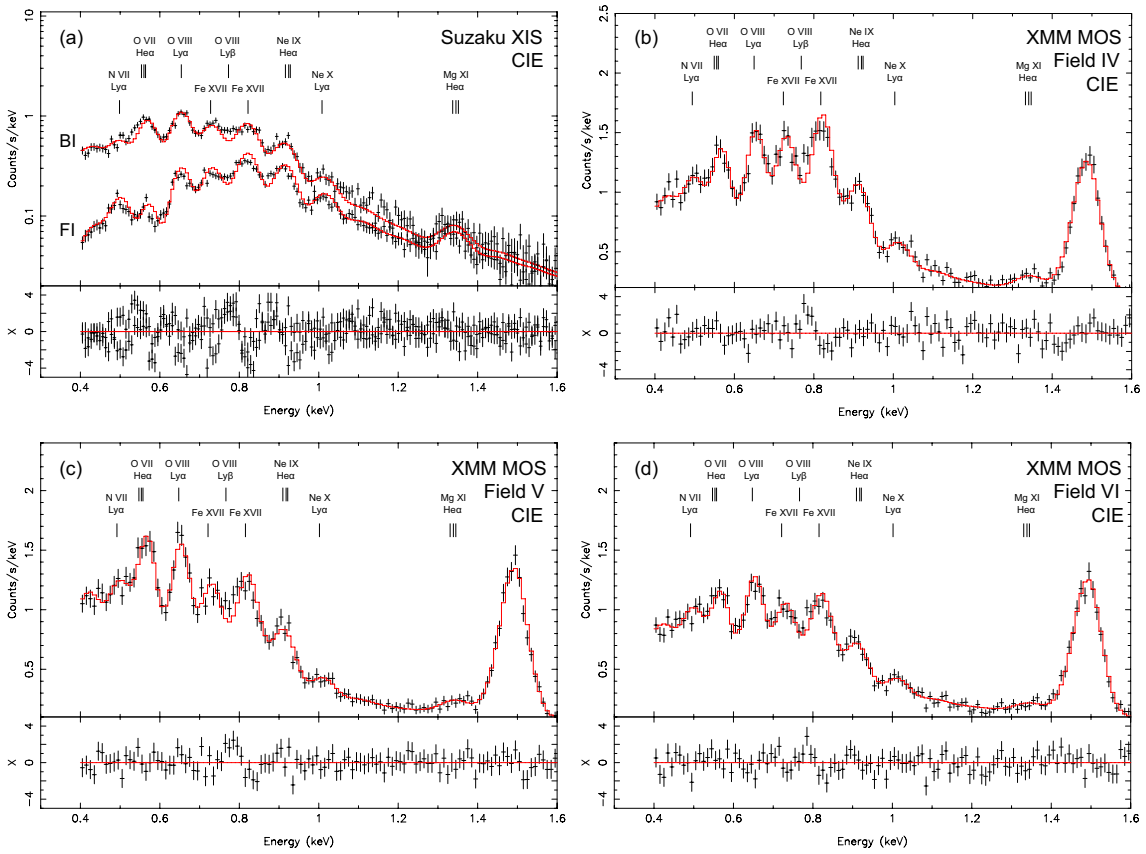

Fig. 1. NPS spectra modeled with a single-phase `CIE` component absorbed by neutral material. The fittings of the *Suzaku* XIS are shown in **a)**, and *XMM-Newton* MOS field IV, V, and VI data are shown in panels **b)**, **c)**, and **d)**, respectively. Strong emission lines are labeled. The line at ≈1.5 keV in each MOS spectrum is an instrumental line.

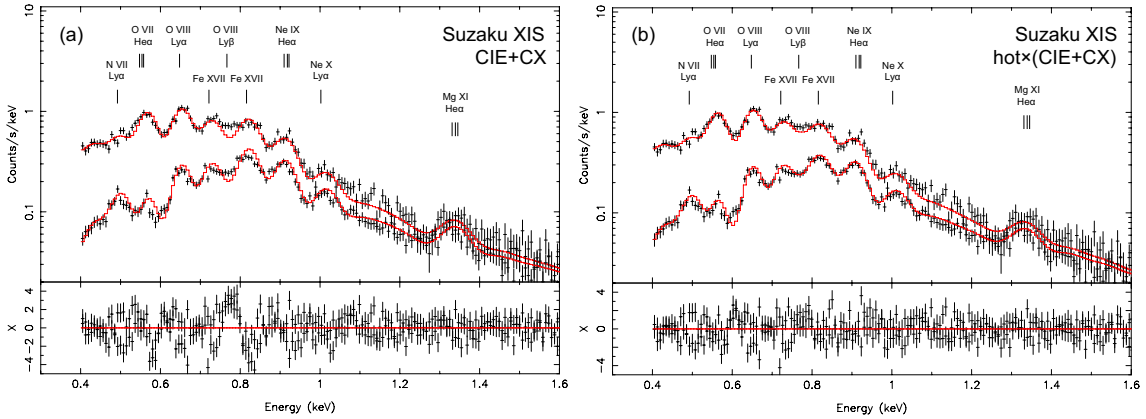

Fig. 2. *Suzaku* NPS spectra modeled with `CIE` + `CX` components absorbed by neutral material **a)**, and absorbed by both neutral and ionized materials **b)**. Strong emission lines are marked in the text.

are 148.8, 130.4, and 126.1 for ≈110 degrees of freedom for field IV, V, and VI, respectively. Compared to the XIS data, the MOS spectra are better fit by the model in the O VII Heα and Ne IX Heα bands, while apparent residuals can still be seen at O VIII Lyβ. The resulting temperatures and metal abundances are presented in Table 1. Similar to the XIS results, the three MOS fields give temperatures of 0.24−0.26 keV, O abundances of ∼0.2−0.3 $Z_\odot$, and Ne, Mg, and Fe values of 0.2−0.7 $Z_\odot$. The best-fit parameters are consistent with those reported in W03.

In some objects, the enhanced forbidden-to-resonance ratios of triplet transitions might be explained by charge-exchange recombination created by highly ionized particles colliding with neutrals (e.g., Dennerl 2010). To examine such a possible component, we included a newly developed `CX` model (Gu et al. 2016) in the spectral fitting. This model calculates charge-exchange emission by incorporating a set of velocity-dependent reaction rates, followed by a radiative cascade calculation up to the atomic shell with principle quantum number $n = 16$. In the fitting, the relative velocity between hot and cold particles was left free to vary, while the ionization temperature and metal abundances of the hot plasma were tied to those of the `CIE` component. As plotted in Fig. 2a, the XIS fitting is slightly improved (ΔC-statistics = 71.2 for a degree of freedom = 715), as the O VII and Ne IX triplets are better reproduced by the recombining

Table 1. Best-fit parameters of the NPS spectra.

		Neutral absorber		Ionized + neutral absorbers	
		CIE	CIE + CX	CIE	CIE + CX
Suzaku XIS	kT^a (keV)	0.27 ± 0.01	0.28 ± 0.01	0.25 ± 0.01	0.25 ± 0.01
	N ($Z_\odot$)	0.71 ± 0.17	0.59 ± 0.12	0.48 ± 0.15	0.49 ± 0.17
	O ($Z_\odot$)	0.25 ± 0.03	0.21 ± 0.04	0.71 ± 0.09	0.65 ± 0.11
	Ne ($Z_\odot$)	0.32 ± 0.03	0.23 ± 0.03	0.48 ± 0.06	0.44 ± 0.07
	Mg ($Z_\odot$)	0.38 ± 0.06	0.25 ± 0.05	0.46 ± 0.08	0.43 ± 0.08
	Fe ($Z_\odot$)	0.54 ± 0.06	0.45 ± 0.04	0.65 ± 0.07	0.63 ± 0.07
	$kT_{\rm hot}{}^b$ (keV)	–	–	0.19 ± 0.01	0.20 ± 0.02
	$nH_{\rm hot}{}^c$ (10^{19} cm^{-2})	–	–	3.8 ± 0.3	5.7 ± 1.3
	C-stat/d.o.f.	1152.9/717	1081.7/715	902.3/714	877.2/712
XMM MOS field IV	kT^a (keV)	0.26 ± 0.01	–	0.24 ± 0.01	–
	O ($Z_\odot$)	0.28 ± 0.05	–	0.68 ± 0.07	–
	Ne ($Z_\odot$)	0.35 ± 0.08	–	0.54 ± 0.07	–
	Mg ($Z_\odot$)	0.70 ± 0.22	–	0.78 ± 0.24	–
	Fe ($Z_\odot$)	0.72 ± 0.07	–	0.74 ± 0.09	–
	$kT_{\rm hot}{}^b$ (keV)	–	–	0.18 ± 0.01	–
	$nH_{\rm hot}{}^c$ (10^{19} cm^{-2})	–	–	3.2 ± 0.3	–
	C-stat/d.o.f.	148.8/111	–	130.5/108	–
XMM MOS field V	kT^a (keV)	0.24 ± 0.01	–	0.23 ± 0.01	–
	O ($Z_\odot$)	0.27 ± 0.06	–	0.62 ± 0.08	–
	Ne ($Z_\odot$)	0.25 ± 0.05	–	0.42 ± 0.07	–
	Mg ($Z_\odot$)	0.62 ± 0.19	–	0.78 ± 0.27	–
	Fe ($Z_\odot$)	0.54 ± 0.06	–	0.59 ± 0.06	–
	$kT_{\rm hot}{}^b$ (keV)	–	–	0.19 ± 0.01	–
	$nH_{\rm hot}{}^c$ (10^{19} cm^{-2})	–	–	2.7 ± 0.4	–
	C-stat/d.o.f.	130.4/109	–	104.3/106	–
XMM MOS field VI	kT^a (keV)	0.25 ± 0.01	–	0.23 ± 0.01	–
	O ($Z_\odot$)	0.23 ± 0.06	–	0.68 ± 0.21	–
	Ne ($Z_\odot$)	0.26 ± 0.07	–	0.61 ± 0.17	–
	Mg ($Z_\odot$)	0.49 ± 0.16	–	0.68 ± 0.29	–
	Fe ($Z_\odot$)	0.56 ± 0.09	–	0.75 ± 0.12	–
	$kT_{\rm hot}{}^b$ (keV)	–	–	0.17 ± 0.02	–
	$nH_{\rm hot}{}^c$ (10^{19} cm^{-2})	–	–	2.8 ± 0.9	–
	C-stat/d.o.f.	126.1/109	–	115.7/106	–

Notes. [(a)] Best-fit plasma temperature of the CIE component. [(b)] Best-fit plasma temperature of the ionized absorber. [(c)] Best-fit column density of the ionized absorber.

component. However, the O VIII Lyβ deficiency cannot be solved with the CX model. Setting the ionization temperature and metal abundances as free parameters has a negligible effect on the fitting. For the MOS spectra, the CIE + CX model does not improve the fitting significantly over the CIE model alone.

Since the observed O VIII Lyman series cannot be described well under the current vision, we measured the O VIII line ratios and compared them directly with the model. This was achieved by ignoring the O VIII ion in the model calculation and replacing it by placing six delta functions at the energies of its Lyα (0.653 keV), Lyβ (0.774 keV), Lyγ (0.817 keV), Lyδ (0.837 keV), Lyϵ (0.847 keV), and Lyζ (0.854 keV). We focus on two types of line ratios, the Lyβ/Lyα, and the (Lyγ + Lyδ + Lyϵ + Lyζ)/Lyβ. As shown in Fig. 3a, the observed Lyβ/Lyα ratios are higher by a factor of 2–3 from different instruments than the value predicted by thin thermal CIE model with a balance temperature below 1.6 keV. The high Lyβ/Lyα can be achieved by the CX model when the collision velocity is lower than about 300 km s^{-1}. This result is consistent with those reported in Cumbee et al. (2016), which shows that the high Lyβ/Lyα ratio of Ne X observed in M82 can be explained by their charge exchange code. Conversely, Fig. 3b shows that the observed (Lyγ + Lyδ + Lyϵ + Lyζ)/Lyβ ratios agree better with the CIE value; the CX value is consistently higher than the observation by a factor of 3–5 for the considered velocity range. The reason is probably that the electrons captured in the O^{8+} + H charge exchange would mainly fall onto the high Rydberg states with n = 4–6, producing strong Lyγ to Lyϵ lines (e.g., Mullen et al. 2016). The n = 3 shell could only be occupied by radiative cascade, and thus Lyβ line is weaker than the combined

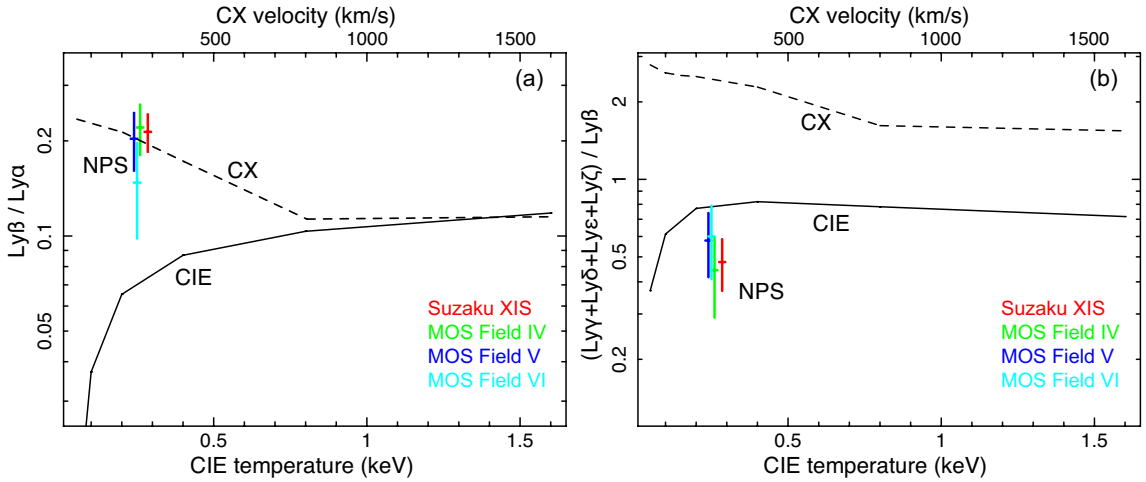

Fig. 3. a) Observed O VIII Lyβ/Lyα ratios obtained with the XIS (red), the MOS field IV (green), field V (blue), and field VI (cyan) plotted against the best-fit temperatures. The solid line is the Lyβ/Lyα versus temperature curve calculated by the `CIE` model, and the dashed line shows the Lyβ/Lyα versus collision velocity by the `CX` model. **b)** Same as panel **a)**, but for the O VIII (Lyγ + Lyδ + Lyϵ + Lyζ)/Lyβ ratio.

transitions from the shells with higher n. The line measurement indicates that neither a pure `CIE` or `CX` nor a combined model can explain the observed NPS spectra.

3.2. Additional ionized absorption

The anomalous Lyβ-to-Lyα ratio leads us to consider another scenario: the emission from the NPS might be obscured in the line of sight by an ionized absorber, so that the transitions with large oscillator strengths, such as resonance lines of the triplets and Lyα lines, are partially absorbed. We used the `hot` model in `SPEX` to calculate the ionized absorption. For a given temperature, it calculates the ionization concentration for each ion and then determines the cross section based on the oscillator strength, the thermal, and turbulent broadening. The plasma transmission is calculated by combining all the ionic transmissions. The ionized absorption was applied, in addition to the neutral absorption, to a `CIE` component describing the NPS emission, as well as to the CXB and GH components. In the fitting, the column density and temperature of the ionized absorber were set free to vary. The average systematic velocity and turbulent broadening of the absorber cannot be determined well by the current data and were always consistent with zero within the error ranges. We therefore assumed the absorber to be nearby and turbulence-free. For a similar reason, the metal abundances of the absorber were fixed to the solar value. As shown in Figs. 4a–d, the new model apparently reproduces the O VIII Lyβ and O VII/Ne IX triplets better for all XIS and MOS spectra. The best-fit C-statistics are 902.3 (degree of freedom = 714) for the XIS, and 130.5, 104.3, and 115.7 (degrees of freedom ≈107) for the three MOS data, significantly better than those obtained in Sect. 3.1. The best-fit XIS model in Fig. 4e indicates that half of the emission in the O VIII Lyα band is absorbed, while the Lyβ emission is absorbed by about 10%.

As presented in Table 1, the ionized absorber has a best-fit temperature of 0.17–0.19 keV, significantly lower than that of the NPS (0.23–0.25 keV). The best-fit column densities by different instruments are in the range of $2.7–3.8 \times 10^{19}$ cm^{-2}. The resulting O abundance of the NPS becomes 0.6–0.7 $Z_\odot$, more than twice the value obtained in Sect. 3.1. The other elements are less affected by the new model, probably because they have lower ionization concentrations than O at the temperature of the absorber. The N/O abundance ratio becomes 0.68 ± 0.22, significantly lower than the one reported in M08 (N/O = 4).

We furthermore investigated the effect of turbulence on the absorption feature in the O VIII bands. The opacity drops with the increasing turbulence, while the absorption line becomes broadened by turbulence so that it would also affect the adjacent continuum. As shown in Fig. 4f, the effective transmittances in near-O VIII Lyα (0.625–0.675 keV) and near-O VIII Lyβ (0.75–0.80 keV) bands are plotted as a function of turbulent velocity. The calculation is based on the best-fit model for the XIS data, including only the O VIII lines and the continuum. The obtained transmittances slightly differ from those shown in Fig. 4e, in which the model is folded with the XIS response. In both energy bands, the absorption feature reaches its maximum at a turbulence of 100–200 km s^{-1} and drops toward lower and higher velocities. As a result, for a turbulent absorber, the column density necessary to fit the observed spectra would be lower by ∼10–20% with respect to the static value at a velocity of 150 km s^{-1}, and becomes almost twice this value at 1000 km s^{-1}.

Next we examined the XIS spectra for the possible charge exchange component. The emission model consists of a `CIE` and a `CX` components, which are both subject to the ionized and neutral absorption. The two emission components have the same temperature and metal abundances, while the collision velocity of the `CX` component is left free. As shown in Fig. 2b and Table 1, the new model provides a minor improvement to the `CIE`-alone fitting, with best-fit C-statistics of 877.2 for a degree of freedom of 712. Based on the best-fit χ^2 values, an F-test shows that the `CX` component is significant on the $>3\sigma$ confidence level. The charge exchange emission contributes ≈8% of the entire NPS emission in 0.3–1.6 keV. The best-fit collision velocity is 150^{+150}_{-100} km s^{-1}. As seen in Table 1, the `CIE` temperature remains intact, while the abundances are slightly affected by including the `CX`. The best-fit N/O ratio becomes 0.75 ± 0.29. The new fitting furthermore prefers a higher column density of the ionized absorption, $5.7 \pm 1.3 \times 10^{19}$ cm^{-2}, to balance the additional line emission introduced by `CX` in the spectra.

4. Discussion

By revisiting the *Suzaku* and *XMM-Newton* data of the NPS region, we discovered that the soft X-ray spectra can be

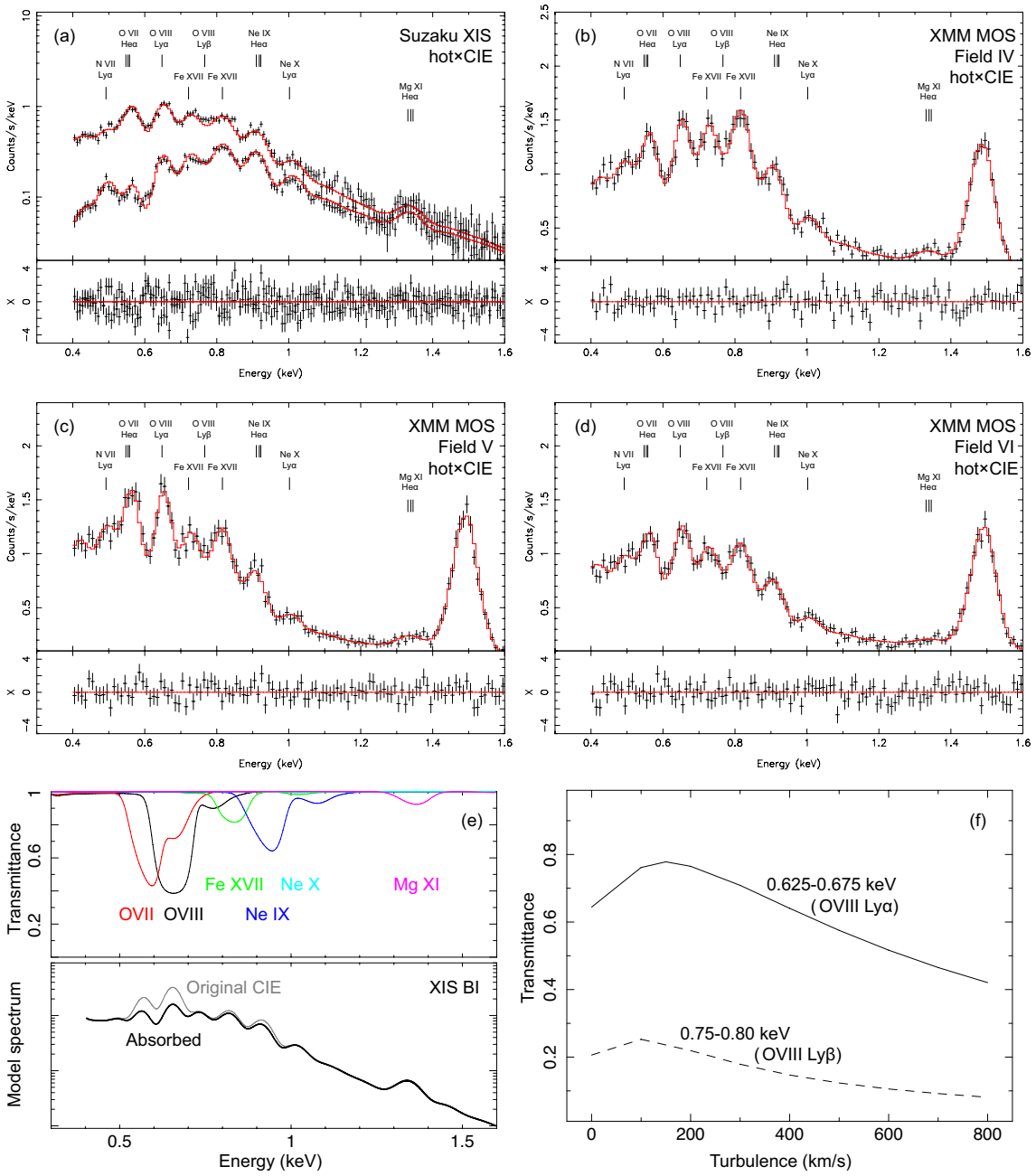

Fig. 4. Same as Fig. 1, but the best-fit models are one CIE component subject to both neutral and ionized absorptions (**a**)–(**d**)). Panel **e)** shows the best-fit O VII, O VIII, Fe XVII, Ne IX, Ne X, and Mg XI transmittances (*upper*), and the best-fit CIE emission absorbed by the ionized particles (*lower*). The model is convolved with the *Suzaku* XIS1 response. Panel **f)** plots the effective transmittances in the near-O VIII Lyα (0.625–0.675 keV; solid line) and near-O VIII Lyβ (0.75–0.80 keV; dashed line) bands as a function of turbulent velocity.

well described by a single-phase thermal component, with a temperature of 0.23–0.25 keV, absorbed by at least two species of foreground materials in both neutral and ionized states. The key evidence for the ionized absorber is the unusually high O VIII Lyβ line relative to other Lyman series. Assuming a nearby turbulent-free plasma, the hot absorber exhibits a balance temperature of 0.17–0.20 keV and column density of $\sim 3-5 \times 10^{19}$ cm^{-2}. A charge-exchange component is marginally detected only with the *Suzaku* XIS data. The oxygen abundance of the NPS is then obtained to be 0.6–0.7 $Z_{\odot}$, apparently higher than those reported in W03 and M08. The Fe/O ratio is consistent with the solar values within measurement uncertainties, while the N/O becomes slightly sub-solar.

Next we shed light on the origin of the ionized absorber based on the derived properties. As shown in Sect. 3.2, the balance temperature of the absorber is 0.17–0.20 keV, lower than the NPS plasma temperature by ≈0.23–0.25 keV on a >90% confidence level. This means that it cannot be fully ascribed to the self-absorption of the NPS plasma. On the other hand, the local hot bubble alone cannot be the absorber either. The temperature of the local hot bubble (≈0.1 keV) is lower than the observed value, and assuming a line-of-sight scale of 40–90 pc and density of 0.01 cm^{-3} (e.g., W03), the column density is estimated to be $1.2-2.7 \times 10^{18}$ cm^{-2}, accounting for <10% of the obtained value (Sect. 3.2).

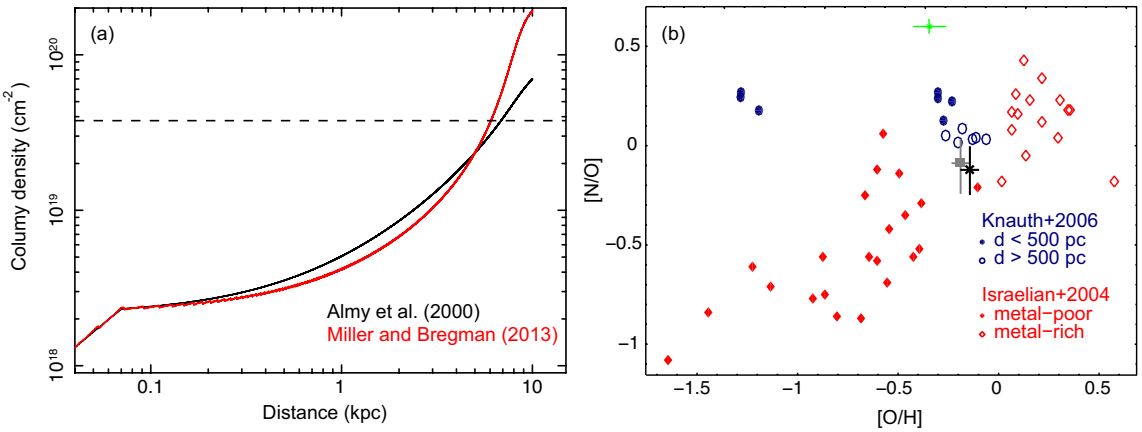

Fig. 5. a) Integrated Earth-centered ISM column density profiles based on the models reported in Almy et al. (2000, black) and Miller & Bregman (2013, red). An additional column density from the local hot bubble is included in the central 70 pc. The dashed line shows the observed value based on the CIE model with ionized absorption. **b)** The [N/O] versus [O/H] diagram. The best-fit NPS results obtained with CIE and CIE plus CX models with the new absorptions are shown with black and gray error bars, respectively. The M08 result is plotted in green. The abundance patterns of the cold ISM based on local star and distant star absorption measurements by Knauth et al. (2006) are plotted as blue filled circles and blue empty circles, respectively. The metal-poor and metal-rich Galactic halo star data from Israelian et al. (2004) are indicated by red filled and red empty diamonds, respectively.

The obtained properties of the ionized absorber are consistent with those reported in the absorption studies on Galactic compact object 4U 1820−303 (Hagihara et al. 2011) and extragalactic objects PKS 2155−304 (Hagihara et al. 2010), LMC X−3 (Yao et al. 2009), and Mrk 509 (Pinto et al. 2012). This leads us to the scenario that the Galactic ISM contributes significantly to the observed ionized absorption. The temperature of ≈0.2 keV appears to be self-consistent with that of the Galactic ISM included as a background component in Sect. 2.2. It also agrees well with previous measurements of the ISM temperature in the Galactic halo (e.g., Smith et al. 2007) and Galactic bulge (e.g., Almy et al. 2000). To calculate the ISM absorption column density, we employed the 3D ISM density models from Almy et al. (2000, in their Fig. 5) and Miller & Bregman (2013, spherical-saturated model in their Table 2). The former is based on *ROSAT* 3/4 keV observation of the emission in the Galactic bulge region, while the latter is focused on the Galactic halo, and used line absorption measurement on background objects. The two models provide galactocentric ISM density profiles, which were then transformed into Earth-centered line-of-sight distance profiles by using Eqs. (1)−(3) of Miller & Bregman (2013). The sky coordinate of the *Suzaku* pointing was used in the center transformation. By integrating the density over distance, we calculated the column density distance profiles and presented them in Fig. 5a. It shows that the two ISM models are roughly consistent with each other. We considered an extreme case, in which the ionized absorption is fully due to the Galactic ISM. Then the models predict that the part of NPS covered by the XIS would be at a distance of ∼6−7 kpc. This is still well in line with the recent measurements of the NPS distance with radio data by Sun et al. (2014) and Sofue (2015).

As described in Sect. 3.2, the higher-than-solar N/O abundance ratio reported in M08 can be migrated to the high opacity of the O VIII Lyα line. In Fig. 5b the new results are plotted in a [N/O] verseus [O/H] diagram and are compared with the abundances of Galactic halo stars measured in Israelian et al. (2004). The NPS values are consistent with the implied Galactic stellar evolution by lying in the gap between the metal-poor and metal-rich subsamples of stars. At the same time, the abundance patterns of Galactic cold ISM, based on HST and FUSE observations of O I and N I absorptions against stars (Knauth et al. 2006) are also plotted in the same diagram of Fig. 5b. Despite the large uncertainties, the NPS results appear to agree better with the abundance patterns of the distant ISM (d > 500 pc) than with those of the local ISM (d < 500 pc). This also supports the scenario that the NPS is a structure in the Galactic halo rather than in the solar neighborhood.

5. Summary

By reanalyzing the *Suzaku* and *XMM-Newton* data of the North Polar Spur, we detected an anomalously high O VIII Lyβ line relative to other Lyman series in four different fields. It prefers an ionized absorption model over a charge exchange component, which suggests that the NPS is partly obscured by foreground plasma, presumably Galactic hot ISM, with a temperature of 0.17−0.20 keV and a column density of $3-5 \times 10^{19}$ cm^{-2}. After correcting for the absorption, the oxygen abundance of the NPS changes from ∼0.2 $Z_\odot$ to ∼0.7 $Z_\odot$, and the abundance ratio between nitrogen and oxygen becomes even slightly lower than the solar value. Combining the absorption and abundance measurements, it is suggested that the North Polar Spur is likely an object in the Galactic halo, supporting the scenario of a Galactic center origin. This exercise provides a good example to show that an accurate spectral model is crucial to ensure reliable scientific output.

Acknowledgements. We thank the referee, Randall Smith, for the valuable comments on the manuscript. SRON is supported financially by NWO, the Netherlands Organization for Scientific Research.

References

Almy, R. C., McCammon, D., Digel, S. W., Bronfman, L., & May, J. 2000, ApJ, 545, 290
Berkhuijsen, E. M., Haslam, C. G. T., & Salter, C. J. 1971, A&A, 14, 252
Bland-Hawthorn, J., & Cohen, M. 2003, ApJ, 582, 246
Cumbee, R. S., Liu, L., Lyons, D., et al. 2016, MNRAS,
Dennerl, K. 2010, Space Sci. Rev., 157, 57
Egger, R. J., & Aschenbach, B. 1995, A&A, 294, L25
Gu, L., Xu, H., Gu, J., et al. 2012, ApJ, 749, 186
Gu, L., Kaastra, J., Raassen, A. J. J., et al. 2015, A&A, 584, L11
Gu, L., Kaastra, J., & Raassen, A. J. J. 2016, A&A, 588, A52
Hagihara, T., Yao, Y., Yamasaki, N. Y., et al. 2010, PASJ, 62, 723

Hagihara, T., Yamasaki, N. Y., Mitsuda, K., et al. 2011, PASJ, 63, S889
Heiles, C., Chu, Y.-H., Troland, T. H., Reynolds, R. J., & Yegingil, I. 1980, ApJ, 242, 533
Israelian, G., Ecuvillon, A., Rebolo, R., et al. 2004, A&A, 421, 649
Kataoka, J., Tahara, M., Totani, T., et al. 2013, ApJ, 779, 57
Katsuda, S., Tsunemi, H., Mori, K., et al. 2011, ApJ, 730, 24
Knauth, D. C., Meyer, D. M., & Lauroesch, J. T. 2006, ApJ, 647, L115
Lallement, R. 2009, Space Sci. Rev., 143, 427
Lisse, C. M., Dennerl, K., Englhauser, J., et al. 1996, Science, 274, 205
Lodders, K., Palme, H., & Gail, H.-P. 2009, Landolt Börnstein
Miller, E. D., Tsunemi Hiroshi, Bautz, M. W., et al. 2008, PASJ, 60, 95 (M08)
Miller, M. J., & Bregman, J. N. 2013, ApJ, 770, 118
Mullen, P. D., Cumbee, R. S., Lyons, D., & Stancil, P. C. 2016, ApJS, 224, 31
Murashima, M., Kokubun, M., Makishima, K., et al. 2006, ApJ, 647, L131
Pinto, C., Kriss, G. A., Kaastra, J. S., et al. 2012, A&A, 541, A147
Smith, R. K., Bautz, M. W., Edgar, R. J., et al. 2007, PASJ, 59, 141
Sofue, Y. 1977, A&A, 60, 327
Sofue, Y. 2015, MNRAS, 447, 3824
Sun, X. H., Gaensler, B. M., Carretti, E., et al. 2014, MNRAS, 437, 2936
Willingale, R., Hands, A. D. P., Warwick, R. S., Snowden, S. L., & Burrows, D. N. 2003, MNRAS, 343, 995 (W03)
Willingale, R., Starling, R. L. C., Beardmore, A. P., Tanvir, N. R., & O'Brien, P. T. 2013, MNRAS, 431, 394
Yao, Y., & Wang, Q. D. 2005, ApJ, 624, 751
Yao, Y., Wang, Q. D., Hagihara, T., et al. 2009, ApJ, 690, 143

Appendix A: Possible problems with the *Suzaku* data calibration

As reported in M08, the *Suzaku* NPS data might be affected by a build-up of contamination on the optical blocking filter in the early phase of the mission. The effective area of the XIS around 0.5 keV is therefore dependent on time and chip location. To examine the possible calibration uncertainty, we analyzed two *Suzaku* datasets observed around the same time as the NPS data, and compared their spectra in the 0.4−1.4 keV band. The two observations were made on 2005 September 21 and 2005 November 2, which pointed to a common target, planetary nebula BD +30 3639. The same data were reported in Murashima et al. (2006).

The XIS data of BD +30 3639 were screened in the same way as described in Sect. 2.1. The source spectra were taken from the central 3′, and the background region was defined as a surrounding annulus with outer radius of 5′. As described in Sect. 2.2, we modeled the background spectrum and corrected for it in the source spectra. The two data were fit simultaneously. As shown in Fig. A.1, the two source spectra are nicely fitted by a CIE model absorbed by Galactic neutral material. The best-fit plasma temperature (0.18 keV) and abundances agree well with those reported in Murashima et al. (2006). The spectrum below 1 keV appears to be more absorbed in the second observation, probably due to the contamination on the optical blocking filter. This effect has been fully corrected for by the response files. This exercise proves that the spectral features on O VII, O VIII, and Ne IX discovered in the NPS data (Sect. 3.1) are probably not due to calibration issues.

Similar to the NPS, the BD +30 3639 spectra also show two prominent Fe XVII lines around, or partially blended with, the O VIII Lyβ line. While the NPS spectra exhibit a strong excess in the O VIII Lyβ line (Sect. 3.1), the same energy band in the BD +30 3639 spectra is well fit by the thermal model. This also indicates that the O VIII Lyβ excess in the NPS is probably not an artifact caused by either Fe XVII blending or poor atomic model calculation of the Fe XVII + O VIII complex.

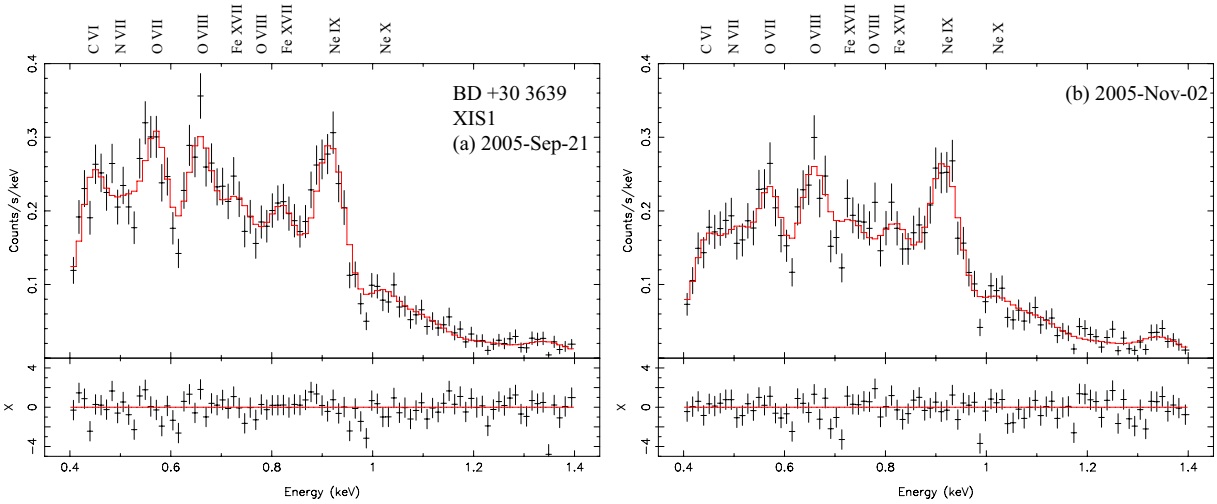

Fig. A.1. XIS1 spectra of BD +30 3639 taken before the NPS **a)** and after the NPS **b)**, modeled with a single-phase CIE component absorbed by Galactic neutral material.